JOURNAL OF SPACECRAFT AND ROCKETS
Vol. 47, No. 3, May–June 2010

Dynamic Modeling of a Wind-Driven Tumbleweed Rover Including Atmospheric Effects

Alexandre E. Hartl* and Andre P. Mazzoleni†
North Carolina State University, Raleigh, North Carolina 27695-7910

DOI: 10.2514/1.45174

A tumbleweed rover is a spherical wind-driven rover designed to explore places of geological interest on the Martian surface. Dynamic models developed for an individual rover are used to create numerical simulations for a rover traversing through flat terrain, a channel, and a crater. The simulations show that the rover's motion is dependent on the terrain type and initial and atmospheric conditions. The results confirm that the wind force both pushes and hinders the rover's motion while sliding, rolling, and bouncing. The rover periodically transitions between these modes of movement when contact is initiated against sloped portions of terrain. Combinations of rolling and bouncing may be a more effective means of transport for a rover traveling through a channel when compared to rolling alone. The aerodynamic effects of drag and the Magnus force are contributing factors to the possible capture of the rover by a crater.

Nomenclature

A	=	cross-sectional area, m^2
b	=	radius, m
C_D	=	drag coefficient
C_L	=	lift coefficient
C_{rr}	=	rolling resistance coefficient
e	=	coefficient of restitution
$\mathbf{F}_D$	=	drag force, $kg \cdot m/s^2$
$\mathbf{F}_{fr}$	=	frictional force, $kg \cdot m/s^2$
$\mathbf{F}_G$	=	gravitational force, $kg \cdot m/s^2$
$\mathbf{F}_M$	=	Magnus force, $kg \cdot m/s^2$
$\mathbf{F}_N$	=	normal force, $kg \cdot m/s^2$
$\mathbf{F}_{rr}$	=	rolling resistance force, $kg \cdot m/s^2$
g	=	gravitational acceleration, m/s^2
J	=	principal moment of inertia, $kg \cdot m^2$
m	=	rover's mass, kg
$\mathbf{n}_i$	=	right-handed unit vector triad defining the Newtonian reference frame ($i = 1, 2, 3$)
q_i	=	generalized coordinate, m ($i = 1, 2, 3$)
S_i	=	component of contact force, $kg \cdot m/s^2$ ($i = 1, 2, 3$)
t	=	time, s
u_i	=	generalized speeds, rad/s ($i = 1, 2, 3$), m/s ($i = 4, 5, 6$)
$\mathbf{v}$	=	velocity of the center of gravity of the rover with respect to the origin, m/s
$\mathbf{v}^P$	=	velocity of the rover at its contact point with a surface, m/s
β	=	angle of inclination, degrees
μ	=	coefficient of static friction
μ'	=	coefficient of kinetic friction
$\boldsymbol{v}_{rel}$	=	relative velocity between the rover and wind velocity, m/s
$\boldsymbol{v}_{wind}$	=	wind velocity vector, m/s
ρ	=	atmospheric density, kg/m^3
$\boldsymbol{\omega}$	=	angular velocity of the rover, rad/s

Received 28 April 2009; revision received 3 February 2010; accepted for publication 8 February 2010.

*Graduate Student, Department of Mechanical and Aerospace Engineering.

†Associate Professor, Department of Mechanical and Aerospace Engineering. Associate Fellow AIAA.

I. Introduction

THE evidence of water on Mars has increased interest in Martian exploration. Future missions will involve the exploration of large areas of the Martian surface, and areas of scientific interest may be far away from the landing sites. Because of the inherent dangers with manned missions, rovers provide an attractive option for investigations of large regions.

NASA currently employs wheeled rovers, including the Mars Exploration Rovers, to examine the Martian surface. These rovers are intricate and expensive, with limited ability to navigate rough terrain [1]. This complicates gathering scientific data on Martian climate and geology, and renders answering questions on the existence of water and life difficult.

A vehicle capable of exploring large areas of terrain is the tumbleweed rover. A tumbleweed is a spherical (wind-driven) rover designed to provide superior mobility and greater accessibility to varied terrains on the surface of Mars. Compared with conventional wheeled rovers, a tumbleweed can cover vast distances faster and reach previously inaccessible areas of scientific interest, such as valleys and craters. Multiple tumbleweeds can be deployed across the Martian surface for scientific surveys. Complementing the data being gathered by satellite remote sensing of subsurface water deposits, the tumbleweed's design is well suited for polar missions, since the rover can seek out water sources beneath a surface desert or an ice sheet by use of microwater sensors [1–9].

This paper's aim is to capture the relevant dynamics needed to describe the motion of a wind-driven spherical rover across the Martian terrain. The dynamic models presented here cover the rover's bouncing, sliding and rolling behaviors and its transition between these modes of movement, where atmospheric effects are taken into account. The increase, or kick, in velocity as a rover rolls over an edge is explored as it may occur when a rover enters a valley or crater. Several simulation examples spotlight how these dynamic models are used to describe a rover's motion while encountering different terrains.

Throughout the study the rover is modeled as a sphere; it is assumed the rover is nonrigid during collisions with the terrain as well as during rolling. The effects of drag and the Magnus force are considered for atmospheres on Earth and Mars.

This paper begins with the development of the equations governing the rover's motion and provides a numerical procedure for their implementation. We then present several simulation examples of a rover encountering various terrain types. We follow with a discussion of how this work may be applied to studies analyzing the rover's motion for particular terrain scenarios.

II. Equations of Motion

A. Bouncing Model

As a rover collides with sloped terrains or impacts rocks in a Martian rock field, its resulting motion will involve intervals of time where it will be airborne. The aerodynamic forces acting on the rover during these intervals and the effects on its trajectory are examined in the following section. Beforehand, a discussion of the rover's collision dynamics is presented.

The general behavior of a bouncing sphere on a flat surface is considered by Kane and Levinson [10]. The model provides a direct method for computing a sphere's generalized speeds after impact considering both the no-slip and slip cases. Figure 1 defines the coordinate system. The angular velocity and the velocity of the sphere's center is expressed in terms of the generalized speeds $u_1, \ldots, u_6$ as

$$\boldsymbol{\omega} = u_1\mathbf{n}_1 + u_2\mathbf{n}_2 + u_3\mathbf{n}_3 \tag{1}$$

and

$$\mathbf{v} = u_4\mathbf{n}_1 + u_5\mathbf{n}_2 + u_6\mathbf{n}_3 \tag{2}$$

For the no-slip case, the equations of motion are

$$u_2(t_2) \approx u_2(t_1) \tag{3}$$

$$u_5(t_2) = -eu_5(t_1) \tag{4}$$

$$u_3(t_2) \approx \frac{Ju_3(t_1) - mbu_4(t_1)}{mb^2 + J} \tag{5}$$

$$u_4(t_2) = -bu_3(t_2) \tag{6}$$

$$u_1(t_2) \approx \frac{Ju_1(t_1) + mbu_6(t_1)}{mb^2 + J} \tag{7}$$

$$u_6(t_2) = bu_1(t_2) \tag{8}$$

$$(S_1^2 + S_3^2)^{1/2} < \mu|S_2| \tag{9}$$

$$S_1 \approx m[u_4(t_2) - u_4(t_1)] \tag{10}$$

$$S_2 \approx m[u_5(t_2) - u_5(t_1)] \tag{11}$$

$$S_3 \approx m[u_6(t_2) - u_6(t_1)] \tag{12}$$

where u_i are the generalized speeds for $i = 1, \ldots, 6$; e is the coefficient of restitution; J is the principal moment of inertia; m is the mass, b is the radius; S_i are the impulses for $i = 1, 2, 3$; and μ is the coefficient of static friction. For no slipping, successive use of Eqs. (3–8) result in a set of values for $u_1, \ldots, u_6$ at time t_2. These values are valid if and only if inequality (9) is satisfied for values of S_1, S_2, and S_3 given by Eqs. (10–12).

Otherwise, if inequality (9) is violated, then the sphere is slipping at time t_2, and the quantities $u_1(t_2)$, $u_3(t_2)$, $u_4(t_2)$, $u_6(t_2)$, S_1, and S_3 must be recalculated using the relationships listed below:

$$\alpha = u_4(t_1) + bu_3(t_1) \tag{13}$$

$$\gamma = u_6(t_1) - bu_1(t_1) \tag{14}$$

$$k = \frac{1}{m} + \frac{b^2}{J} \tag{15}$$

$$S_1 \approx -\mu'|S_2|\frac{\alpha + kS_1}{|\alpha + kS_1|[1 + (\gamma/\alpha)^2]^{1/2}} \tag{16}$$

$$S_3 \approx \frac{\gamma_1}{\alpha_1}S_1 \tag{17}$$

$$u_1(t_2) \approx u_1(t_1) - bS_3/J \tag{18}$$

$$u_3(t_2) \approx u_3(t_1) + bS_1/J \tag{19}$$

$$u_4(t_2) \approx u_4(t_1) + S_1/m \tag{20}$$

$$u_6(t_2) \approx u_6(t_1) + S_3/m \tag{21}$$

where α, γ, and k are constants and μ' is the coefficient of kinetic friction. Note that $u_1(t_2)$, $u_5(t_2)$, and S_2 are given by Eqs. (3), (4), and (11), respectively, regardless of whether or not the sphere experiences no slipping or slipping at time t_2. Figure 2 presents the algorithm as a flow chart.

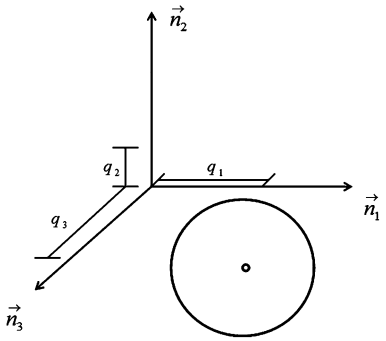

Fig. 1 Coordinate axes.

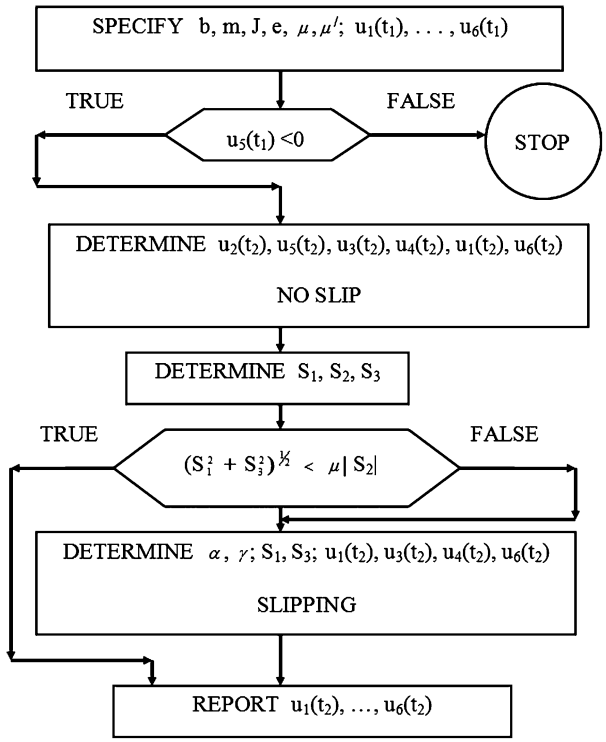

Fig. 2 Bounce algorithm as developed by Kane and Levinson [10].

We extend the bouncing model to include collisions on inclined and declined surfaces and we account for the drag and Magnus force acting on the sphere between bounces. Note that in adapting the equations used by Kane and Levinson [10] for sloping surfaces, several modifications are made to the model. First, the reinitialization of the sphere's generalized speeds after impact must now account for the gravity components acting parallel and normal to the plane. Moreover, the collision detection between the sphere and surface can no longer be determined analytically, but must now be tracked numerically. These tasks are most easily accomplished by introducing a trajectory model within the bouncing model, and this technique is used in this study.

B. Trajectory Model

For a sphere moving through air, its motion is affected by gravity, air resistance (drag) and additional aerodynamic forces due to its spinning motion (the Magnus effect). The force of gravity acting on the sphere is defined as follows:

$$\mathbf{F}_G = -mg\mathbf{n}_2 \tag{22}$$

where m is the sphere's mass and g is the acceleration due to gravity.

The forces on a spinning sphere that is flying through the air are generally divided into two types: a drag force and a lift force. The drag force acts in the opposite direction to the path of the sphere. The lift force is the upwards or sidewards force that is responsible for the Magnus effect.

First, we define the relative velocity of the sphere, and this determines whether the wind drag pushes or resists the sphere's motion:

$$\begin{aligned}\boldsymbol{v}_{\text{rel}} &= \boldsymbol{v}_{\text{sphere}} + \boldsymbol{v}_{\text{wind}} = (u_4 - v_{\text{wind},q_1})\mathbf{n}_1 + (u_5 - v_{\text{wind},q_2})\mathbf{n}_2 \\ &\quad + (u_6 - v_{\text{wind},q_3})\mathbf{n}_3 = (u_{4,\text{rel}})\mathbf{n}_1 + (u_{5,\text{rel}})\mathbf{n}_2 + (u_{6,\text{rel}})\mathbf{n}_3\end{aligned} \tag{23}$$

where $u_{4,\text{rel}} = u_4 - v_{\text{wind},q_1}$, $u_{5,\text{rel}} = u_5 - v_{\text{wind},q_2}$, and $u_{6,\text{rel}} = u_6 - v_{\text{wind},q_3}$. The drag force may be written as

$$\mathbf{F}_D = -\tfrac{1}{2}\rho A C_D |\boldsymbol{v}_{\text{rel}}| \boldsymbol{v}_{\text{rel}} \tag{24}$$

where ρ is the atmospheric density, A is the sphere's cross-sectional area, and C_D is the drag coefficient [11]. In scalar form the equations become

$$F_{D,q_1} = -\tfrac{1}{2}\rho A C_D |\boldsymbol{v}_{\text{rel}}| u_{4,\text{rel}} \tag{25}$$

$$F_{D,q_2} = -\tfrac{1}{2}\rho A C_D |\boldsymbol{v}_{\text{rel}}| u_{5,\text{rel}} \tag{26}$$

$$F_{D,q_3} = -\tfrac{1}{2}\rho A C_D |\boldsymbol{v}_{\text{rel}}| u_{6,\text{rel}} \tag{27}$$

where F_{D,q_1}, F_{D,q_2}, and F_{D,q_3} are the components of $\mathbf{F}_D$ in the $\mathbf{n}_1$, $\mathbf{n}_2$, and $\mathbf{n}_3$ directions, respectively.

The Magnus Force is the force that causes spinning objects to have lateral deflections. Let $\boldsymbol{v}_{\text{rel}}$ again be the sphere's relative velocity and let $\boldsymbol{\omega}$ be the rate at which the sphere spins. The effect of the Magnus force is orthogonal to the velocity and spin of the sphere, and its direction is determined by the cross product of $\boldsymbol{\omega} \times \boldsymbol{v}_{\text{rel}}$. The Magnus force may be written as

$$\begin{aligned}\mathbf{F}_M &= \frac{1}{2}\rho A C_L \frac{|\boldsymbol{v}_{\text{rel}}|}{|\boldsymbol{\omega}|}\boldsymbol{\omega} \times \boldsymbol{v}_{\text{rel}} = \left[\frac{1}{2}\rho A C_L \frac{|\boldsymbol{v}_{\text{rel}}|}{|\boldsymbol{\omega}|}\right](u_1\mathbf{n}_1 + u_2\mathbf{n}_2 \\ &\quad + u_3\mathbf{n}_3) \times (u_{4,\text{rel}}\mathbf{n}_1 + u_{5,\text{rel}}\mathbf{n}_2 + u_{6,\text{rel}}\mathbf{n}_3)\end{aligned} \tag{28}$$

where C_L is the lift coefficient [12]. In scalar form the equations are

$$F_{M,q_1} = \frac{1}{2}\rho A C_L \frac{|\boldsymbol{v}_{\text{rel}}|}{|\boldsymbol{\omega}|}(u_2 u_{6,\text{rel}} - u_3 u_{5,\text{rel}}) \tag{29}$$

$$F_{M,q_2} = \frac{1}{2}\rho A C_L \frac{|\boldsymbol{v}_{\text{rel}}|}{|\boldsymbol{\omega}|}(u_3 u_{4,\text{rel}} - u_1 u_{6,\text{rel}}) \tag{30}$$

$$F_{M,q_3} = \frac{1}{2}\rho A C_L \frac{|\boldsymbol{v}_{\text{rel}}|}{|\boldsymbol{\omega}|}(u_1 u_{5,\text{rel}} - u_2 u_{4,\text{rel}}) \tag{31}$$

where F_{M,q_1}, F_{M,q_2}, and F_{M,q_3} are the components of $\mathbf{F}_M$ in the $\mathbf{n}_1$, $\mathbf{n}_2$, and $\mathbf{n}_3$ directions, respectively.

Consequently, the resultant force on the sphere while airborne is

$$\mathbf{F} = \mathbf{F}_G + \mathbf{F}_D + \mathbf{F}_M \tag{32}$$

During simulations, the trajectory model numerically tracks the sphere's motion between bounces and detects when a collision occurs between the sphere and the terrain. When a collision is detected, the sphere's position and velocities are reset using linear interpolation.

C. Rolling/Sliding Model

Consider a sphere moving on the surface shown in Fig. 3. Its position and velocity are defined as

$$\mathbf{q} = q_1\mathbf{c}_1 + q_2\mathbf{c}_2 + q_3\mathbf{c}_3 \tag{33}$$

and

$$\boldsymbol{\omega} = u_1\mathbf{c}_1 + u_2\mathbf{c}_2 + u_3\mathbf{c}_3 \tag{34}$$

$$\mathbf{v} = u_4\mathbf{c}_1 + u_5\mathbf{c}_2 + u_6\mathbf{c}_3 \tag{35}$$

The force acting on the sphere is

$$\mathbf{F} = \mathbf{F}_G + \mathbf{F}_N + \mathbf{F}_D + \mathbf{F}_{\text{rr}} + \mathbf{F}_{\text{fr}} \tag{36}$$

where

$$\begin{aligned}\mathbf{F}_G &= -mg(\cos\beta\mathbf{c}_2 - \sin\beta\mathbf{c}_3) \\ \mathbf{F}_N &= N\mathbf{c}_2 \\ \mathbf{F}_D &= \frac{1}{2}\rho A C_D |\boldsymbol{v}_{\text{rel}}| \boldsymbol{v}_{\text{rel}}\end{aligned} \tag{37}$$

and $\mathbf{F}_{\text{rr}}$ and $\mathbf{F}_{\text{fr}}$ are described below.

When the sphere is rolling, the rolling resistance is given by

$$\mathbf{F}_{\text{rr}} = -C_{\text{rr}}|N|\left(\frac{\boldsymbol{v}}{|\boldsymbol{v}|}\right) \tag{38}$$

where C_{rr} is the rolling resistance coefficient. For a sphere at rest or slipping, $\mathbf{F}_{\text{rr}} = 0$.

In addition to rolling resistance $\mathbf{F}_{\text{rr}}$, the frictional forces (due to static or kinetic friction) for a rolling sphere is given by

$$\mathbf{F}_{\text{fr}} = F_{\text{fr},q_1}\mathbf{c}_1 + F_{\text{fr},q_3}\mathbf{c}_3 \tag{39}$$

where F_{fr,q_1} and F_{fr,q_3} are components of friction acting in the $\mathbf{c}_1$ and $\mathbf{c}_3$ directions, respectively, and whose values are determined below. If the sphere is sliding,

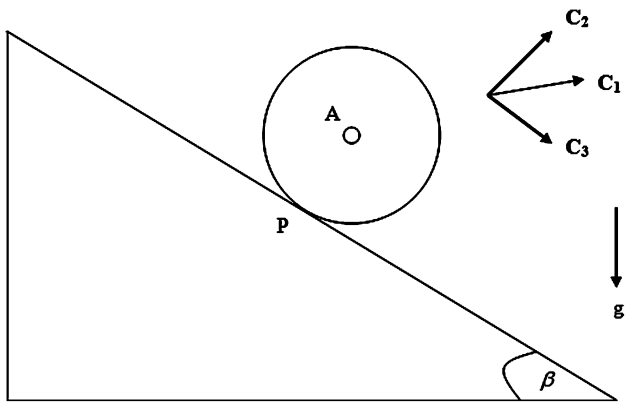

Fig. 3 Sphere moving on a declined surface.

$$\mathbf{F}_{\text{fr}} = -\mu' |N| \left(\frac{\boldsymbol{v}_P}{|\boldsymbol{v}_P|} \right) \tag{40}$$

where the velocity $\boldsymbol{v}_P$ of the contact point of the sphere with the decline is given at all times by

$$\boldsymbol{v}_P = \boldsymbol{v} + \boldsymbol{\omega} \times \mathbf{p} = (u_4 \mathbf{c}_1 + u_6 \mathbf{c}_3) + (u_1 \mathbf{c}_1 + u_2 \mathbf{c}_2 + u_3 \mathbf{c}_3) \times -b\mathbf{c}_2 = (u_4 + bu_3)\mathbf{c}_1 + (u_6 - bu_1)\mathbf{c}_3 = v_{P,1}\mathbf{c}_1 + v_{P,3}\mathbf{c}_3 \tag{41}$$

where $v_{P,1} = u_4 + bu_3$ and $v_{P,3} = u_6 - bu_1$. Note that $\boldsymbol{v}_P \cdot \mathbf{c}_2 = 0$, since point P is the contact point; note also that $u_5 = 0$, since for the contact point there is no velocity in the vertical direction.

The moment acting on the sphere due to the friction force is

$$\mathbf{M} = \mathbf{p} \times \mathbf{F}_{\text{fr}} = -b\mathbf{c}_2 \times (F_{\text{fr},q_1}\mathbf{c}_1 + F_{\text{fr},q_3}\mathbf{c}_3) = -bF_{\text{fr},q_3}\mathbf{c}_1 + bF_{\text{fr},q_1}\mathbf{c}_3 \tag{42}$$

For rolling without slipping, there are two additional constraints on $\boldsymbol{v}_P$; namely, $v_{P,1} = 0$ and $v_{P,3} = 0$. Consequently,

$$u_4 = -bu_3 \tag{43}$$

$$u_6 = bu_1 \tag{44}$$

Taking the time derivatives of u_4 and u_6, respectively, gives the following relations:

$$\dot{u}_4 = -b\dot{u}_3 \tag{45}$$

$$\dot{u}_6 = b\dot{u}_1 \tag{46}$$

Application of Newton's second law yields

$$\dot{u}_1 = (-bF_{\text{fr},q_3})/J \tag{47}$$

$$\dot{u}_2 = 0 \tag{48}$$

$$\dot{u}_3 = (bF_{\text{fr},q_1})/J \tag{49}$$

$$\dot{u}_4 = (F_{\text{fr},q_1} + F_{D,q_1} + F_{\text{rr},q_1})/m \tag{50}$$

$$\dot{u}_5 = 0 = (N - mg\cos\beta)/m \tag{51}$$

$$\dot{u}_6 = (F_{\text{fr},q_3} + F_{D,q_3} + F_{\text{rr},q_3} + mg\sin\beta)/m \tag{52}$$

To solve these equations for the no-slip case, we first determine the angular accelerations $\dot{u}_1$, $\dot{u}_2$, and $\dot{u}_3$. By Eq. (48),

$$\dot{u}_2 = 0 \tag{53}$$

To solve for $\dot{u}_1$, substitute Eq. (46) into Eq. (52) and multiple both sides by $-b$. Then we solve the resulting equation as well as Eq. (47) for $-bF_{\text{fr},q_3}$ and set them equal to each other. Solving for $\dot{u}_1$ yields

$$\dot{u}_1 = \frac{b(F_{D,q_3} + F_{\text{rr},q_3} + mg\sin\beta)}{J + mb^2} \tag{54}$$

Following a similar procedure, $\dot{u}_3$ is

$$\dot{u}_3 = \frac{-b(F_{D,q_1} + F_{\text{rr},q_1})}{J + mb^2} \tag{55}$$

F_{fr,q_1} and F_{fr,q_3} can be shown to be

$$F_{\text{fr},q_1} = \frac{-J(F_{D,q_1} + F_{\text{rr},q_1})}{J + mb^2} \tag{56}$$

$$F_{\text{fr},q_3} = \frac{-J(F_{D,q_3} + F_{\text{rr},q_3} + mg\sin\beta)}{J + mb^2} \tag{57}$$

Numerically, the assumption of no slipping must be checked at each time step. Recall that no slipping occurs provided

$$(F_{\text{fr},q_1}^2 + F_{\text{fr},q_3}^2)^{1/2} < \mu |N| \tag{58}$$

where $N = mg\cos\beta$. As long as the inequality is satisfied, the sphere is rolling. Otherwise, the sphere is slipping and a new a set of equations is required.

For slipping, Eqs. (47–52) are still valid, but $\mathbf{F}_{\text{rr}} = 0$. Also, the constraints $v_{P,1} = 0$ and $v_{P,3} = 0$ no longer hold and the frictional force is given solely by Eq. (40). Figure 4 presents the algorithm for determining whether the sphere is rolling or slipping at each time step. Note that the equations of motion for flat and inclined surfaces may be derived following a similar procedure. Letting $\beta = 0$ will generate the equations of motion for a flat surface. For an inclined surface, note that the gravity component acting parallel to the surface will be negative.

D. Edge Model

The behavior of a ball rolling off the edge of a table is considered in a paper by Bacon [13]. For small velocities, a kick is given to the ball as it rolls off the edge. The kick results in an increase in the ball's horizontal velocity and occurs only if the ball rotates about the edge. At higher velocities no kick is given to the ball. The numerical solution to this problem involves an initial no-slip phase followed by a short slipping phase (see Fig. 5). This problem is important because this event may occur when a rover enters a valley or crater.

For the no-slip phase, the equations of motion are

$$\frac{F_N}{m} = g\sin\theta - b\dot{\theta}^2 \tag{59}$$

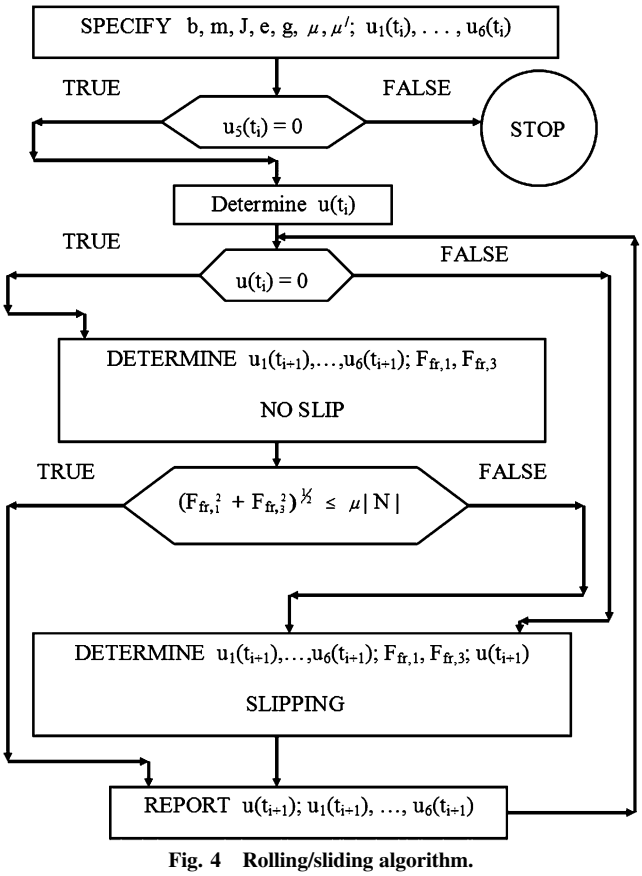

Fig. 4 Rolling/sliding algorithm.

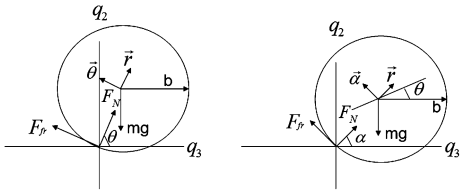

Fig. 5 Free body diagrams.

$$\frac{F_{\text{fr}}}{m} = g\cos\theta + b\ddot{\theta} \tag{60}$$

$$\ddot{\theta} = -\frac{g\cos\theta}{b + \frac{J}{mb}} \tag{61}$$

where F_N is the normal force, F_{fr} is the frictional force, θ is the angle of the ball's rotation, g is the acceleration due to gravity, and J is the principal moment of inertia. These equations are valid as long as $F_{\text{fr}}/F_N \leq \mu$, where μ is the coefficient of static friction. Note that the range of angular velocities for which a kick occurs is $\omega < \sqrt{g/b}$.

Once the ratio F_{fr}/F_N exceeds μ, the ball begins to slip and the equations of motion become

$$\frac{F_N}{m} = g\sin\alpha - b\dot{\alpha}^2 \tag{62}$$

$$\frac{F_{\text{fr}}}{m} = g\cos\alpha + b\ddot{\alpha} \tag{63}$$

$$\ddot{\alpha} = -(g/b)(\cos\alpha - \mu'\sin\alpha) - \mu'\dot{\alpha}^2 \tag{64}$$

$$\ddot{\theta} = -\left(\frac{mb}{J}\right)\left(\frac{F_{\text{fr}}}{m}\right) \tag{65}$$

where α defines the angle of the ball's center of mass relative to an origin fixed at the edge, θ is the angle of rotation of the ball, and μ' is the coefficient of kinetic friction. The slip phase of the ball's motion concludes when $F_N/m = 0$, the condition that indicates that the ball is leaving the table.

As an example, consider a standard golf ball[‡] ($b = 0.0213$ m) and assume the following parameter values: $g = 9.81$ m/s^2, $J/m = 0.4b^2$, $\mu = 0.22$, and $\mu' = 0.20$. Figure 6 shows the initial and final angular velocities of the ball and Fig. 7 displays the initial angular velocity and the ball's angle of rotation when it leaves the table. For comparison, both the no-slip case and the slip case are included in the figures. The straight horizontal and vertical lines represent the upper limit on the angular velocity $\omega = \sqrt{g/b}$ for which a kick no longer occurs. As expected, the kick given to the ball is smaller in the slip case but is larger if it is assumed that the initial and final angular velocities are equal.

To account for balls rolling off tables with edge angles less than 90° (see Fig. 8), an addition to Bacon's numerical procedure is required. A collision detection test is added to determine if the ball collides with the declined plane before losing contact with the table's edge. If this event occurs, the amount of kick given to the ball will depend on whether the collision takes place during the no-slip or slip phase, the angle of the ball's rotation and the angle of the edge. Figure 9 shows the initial and final angular velocities and Fig. 10 displays the initial angular velocity and the ball's angle of rotation for edge angles of 5, 20, and 60°. Note that for an edge angle of 60°, there is no collision with the declined plane.

The algorithm for the edge model for the no-slip and slip cases as well as the collision detection test are shown in Fig. 11. For balls rolling up the edge of a table, several minor modifications to the equations previously presented are required.

[‡]Data available online at http://www.onlygolfballs.com/msg11.htm [retrieved 9 December 2008].

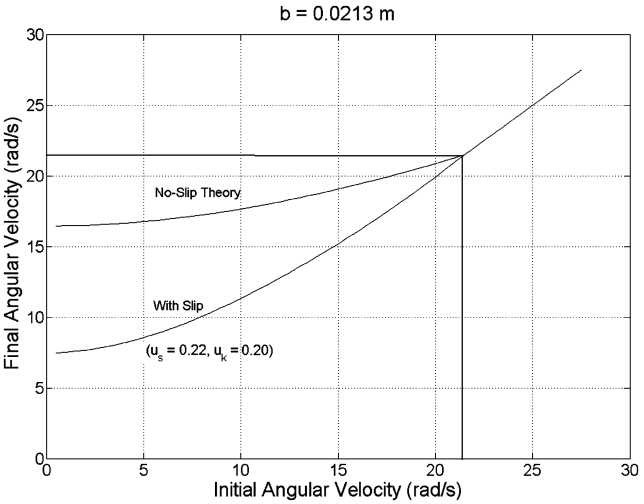

Fig. 6 Final versus initial angular velocity considering both the slip and no-slip cases.

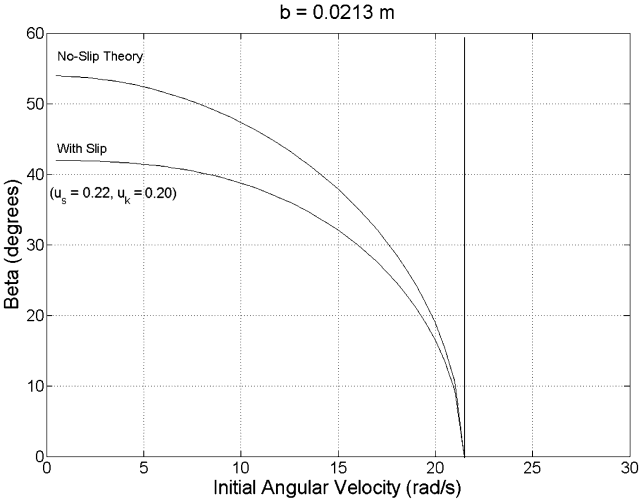

Fig. 7 Angle ball rotates before losing contact with the table's edge considering both the slip and no-slip cases.

III. Simulations

Three simulation examples are given to illustrate how the model presented in this paper can be used to study tumbleweed rover dynamics and performance. The first example considers the rover's motion on flat terrain on Earth, and the second and third examples concern a channel and crater, respectively, on Mars. Note that the models are completely general for flat and sloping surfaces and can

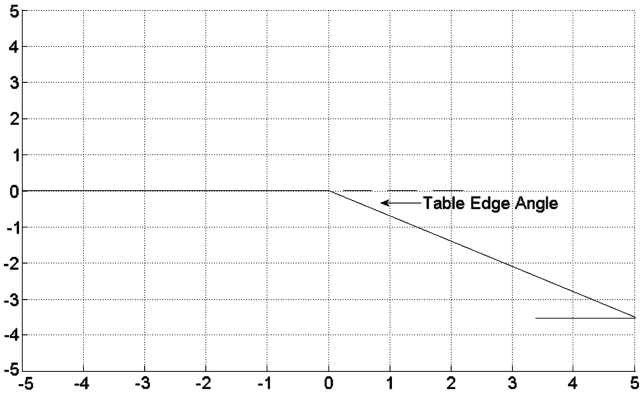

Fig. 8 Table's edge angle.

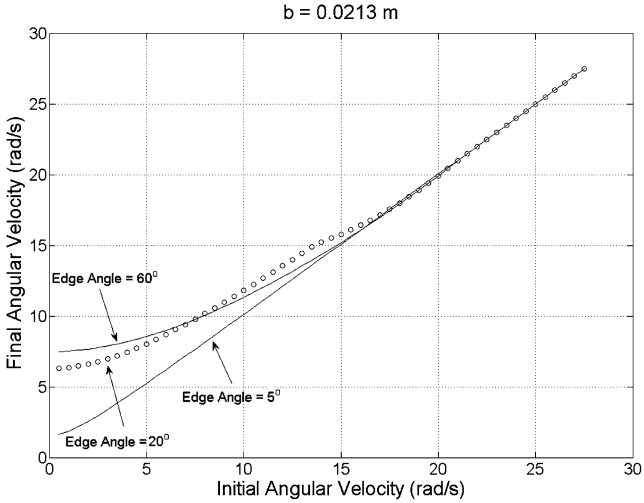

Fig. 9 Final versus initial angular velocity.

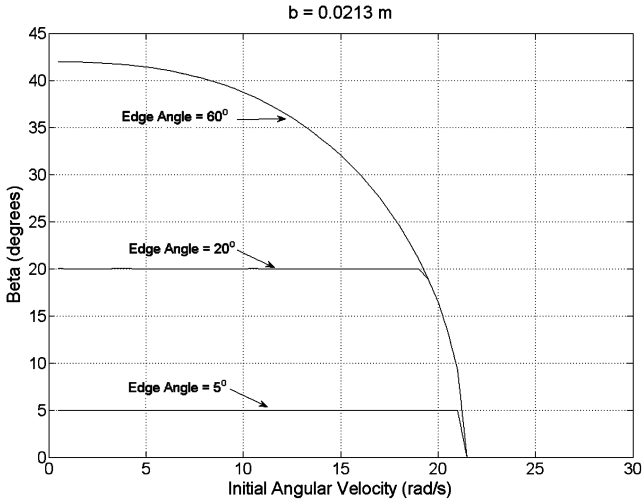

Fig. 10 Angle ball rotates before losing contact with the table's edge.

be applied to a number of terrain scenarios by use of appropriate coordinate transformations. The gravitational, atmospheric, and wind conditions for Earth and Mars are obtained from literature [1,14], and the rover's physical parameters and initial conditions for each example are summarized in Tables 1–3. For all examples the rolling resistance coefficient is $C_{rr} = 0.1$ for soft sand or $C_{rr} = 0.3$ for sandy dirt [14].

Table 1 Physical conditions, properties, and initial conditions used in example 1

Property	Value
Atmospheric density, kg/m^3	1.2
Drag coefficient	0.5
Gravity, m/s^2	9.81
Coefficient of static friction	0.1
Coefficient of kinetic friction	0.08
Coefficient of elasticity	0.8
Rolling resistance	0.1
Rover mass, kg	20
Radius, m	5
Principal moment of inertia, kg-m^2	200
u_1, rad/s	0
u_2, rad/s	0
u_3, rad/s	0
u_4, m/s	0
u_5, m/s	0
u_6, m/s	0

A. Example 1

The first example displays the effect of wind on the rover's motion as it slides and rolls on a flat surface on the Earth. A wind model similar to the one presented in a paper by Rose et al. [14] is used, in which our wind model has a larger magnitude and is run over a shorter duration. The wind starts in the $\mathbf{n}_3$ direction, then sweeps back and forth between the $\mathbf{n}_1$ and $\mathbf{n}_3$ directions, before returning to a state of no wind (see Fig. 12). The wind model is defined as a function of time by $v_{\text{wind},q_1} = 7 \sin 18t$ and $v_{\text{wind},q_3} = 7 \cos 18t$, and is chosen to show the effects of changing wind on the rover's motion. The resultant wind force is directed toward the rover's center of mass. Figure 13 displays the path of the rover's contact point with the wind velocity vectors superimposed. The parameters and initial conditions used in the simulation are given in Table 1. In the simulation the rover is initially at rest, then slides and rolls until the rolling resistance force becomes dominant, stopping the rover's forward progression. As expected, the drag force both hinders and pushes the rover in the q_1 and q_3 directions, and these effects depend on the relative velocity between the rover and the wind.

Figure 14 shows the rover's initial slip phase and its transition to rolling, and Fig. 15 displays the frictional force vectors acting on the rover. Note the abrupt magnitude change of the frictional force vectors when the rover transitions between slipping and rolling.

Table 2 Physical conditions, properties, and initial conditions used in example 2

Property	Case I	Case II
Atmospheric density, kg/m^3	0.0155	0.0155
Drag coefficient	0.5	0.5
Lift coefficient	0.2	0.2
Gravity, m/s^2	3.71	3.71
Coefficient of static friction	0.1	0.1
Coefficient of kinetic friction	0.08	0.08
Coefficient of elasticity	0.8	0.8
Rolling resistance	0.1	0.1
Rover mass, kg	20	20
Radius, m	2	2
Principal moment of inertia, kg-m^2	32	32
u_1, rad/s	−1.5	0
u_2, rad/s	0	0
u_3, rad/s	−3.5	−3.808
u_4, m/s	7	7.616
u_5, m/s	0	0
u_6, m/s	−3	0

Table 3 Physical conditions, properties, and initial conditions used in example 3

Property	Case I	Case II	Case III
Atmospheric density, kg/m^3	0.0155	0	0.0155
Drag coefficient	0.5	0	0.5
Lift coefficient	0.2	0	0.2
Gravity, m/s^2	3.71	3.71	3.71
Coefficient of static friction	0.1	0.1	0.1
Coefficient of kinetic friction	0.080	0.080	0.080
Coefficient of elasticity	0.8	0.85	0.85
Rolling resistance	0.1	0.3	0.3
Rover mass, kg	20	20	20
Radius, m	3	3	3
Principal moment of inertia, kg-m^2	72	72	72
u_1, rad/s	1.67	2.77	2.77
u_2, rad/s	0	0	0
u_3, rad/s	−0.83	−0.67	−0.67
u_4, m/s	2.5	2	2
u_5, m/s	0	0	0
u_6, m/s	5	8.3	8.3

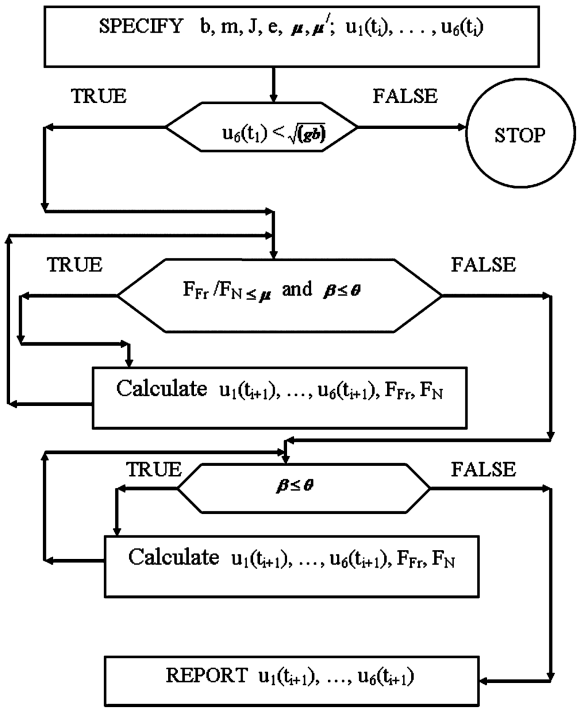

Fig. 11 Edge algorithm.

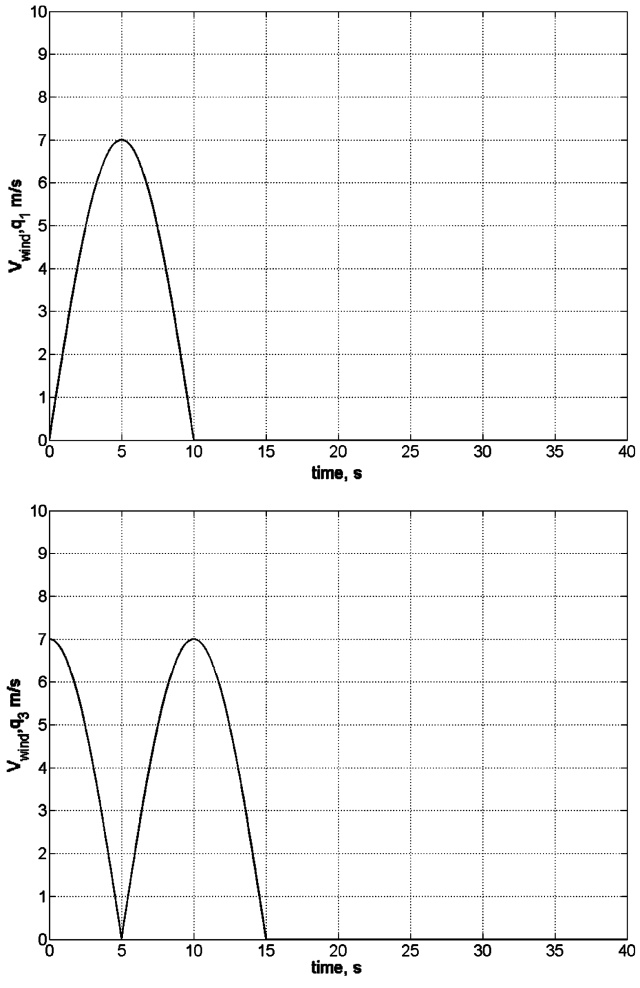

Fig. 12 Vector components of the wind velocity.

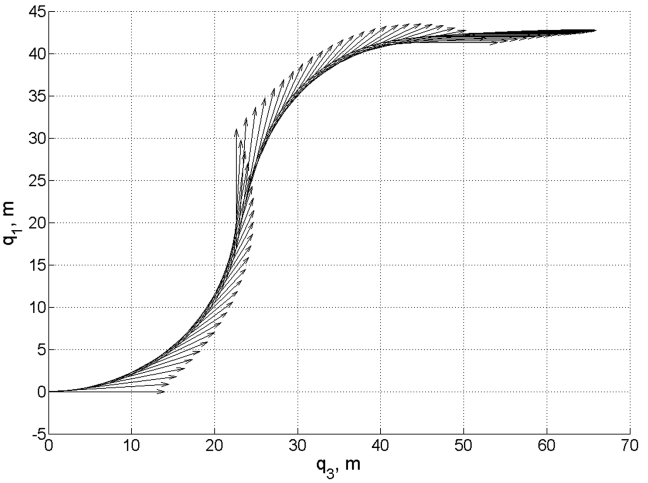

Fig. 13 Path of the rover's contact point with wind velocity vectors superimposed.

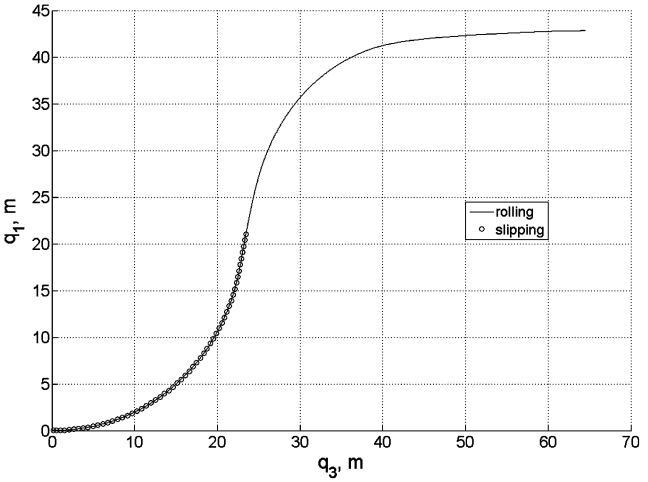

Fig. 14 Path of the rover's contact point showing slipping and rolling modes.

B. Example 2

The second example examines the behavior of a rover as it negotiates a channel on Mars. It also verifies the numerical procedure for detecting collisions and switching between different modes of movement (i.e., sliding, rolling, and bouncing).

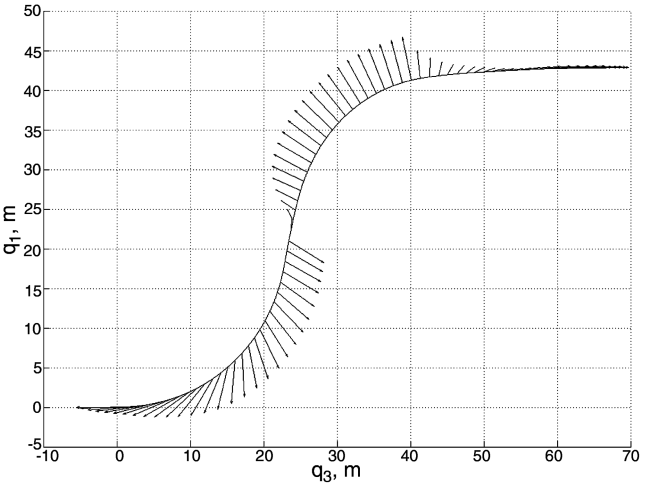

Fig. 15 Path of the rover's contact point with frictional force vectors superimposed.

Many natural channels are approximately trapezoidal and they are characterized by their depth, base width, and left/right side slope [15], as illustrated in Fig. 16.

Figure 17 depicts the rover's motion through a channel and it shows the simulation in both a three-dimensional and topographic view. The channel parameters are listed in Fig. 16 and the parameters and initial conditions used in the simulation are given in Table 2. The rover is initially given a velocity in both the q_1 and q_3 directions to ensure that collisions occur between the rover and the channel's side slopes during the simulation. In this example there is no wind force acting on the rover. Note that the line segments indicate sliding or rolling while bouncing is indicated by a series of images of the rover, which show where it contacts the terrain. As expected, the rover rolls and bounces and alternates periodically between these two modes of movement before coming to a stop. For comparison, Fig. 18 repeats

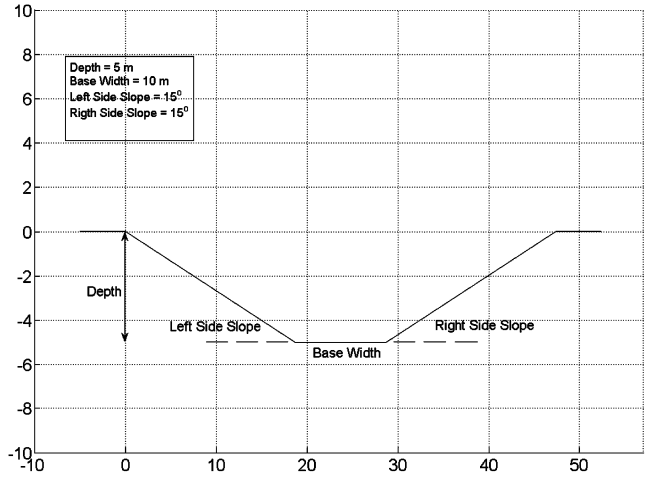

Fig. 16 Channel cross section.

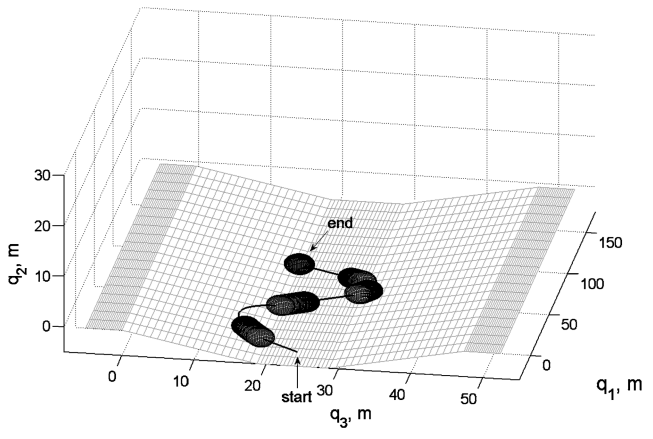

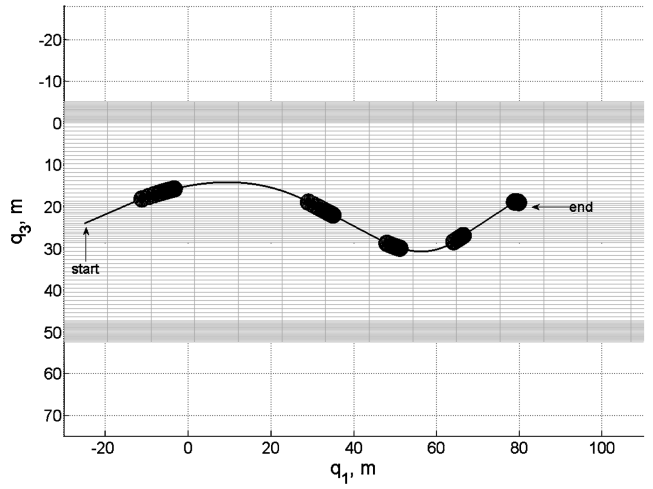

Fig. 17 Case I: a rover moving through a channel; circles denote bounce and the line denotes rolling/sliding.

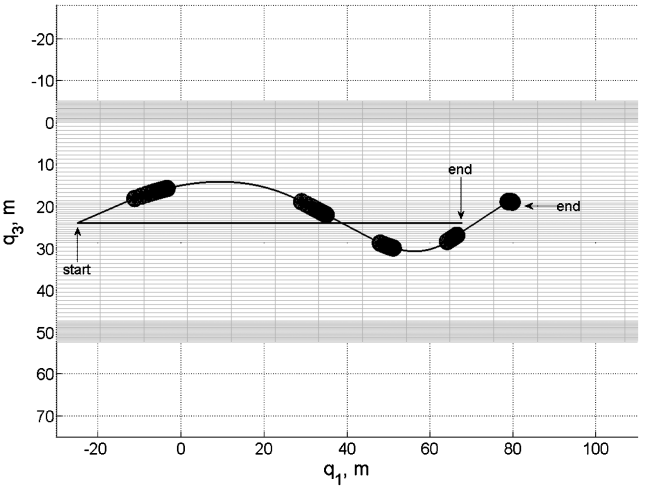

Fig. 18 Case II: a rover moving through a channel; the line denotes rolling/sliding.

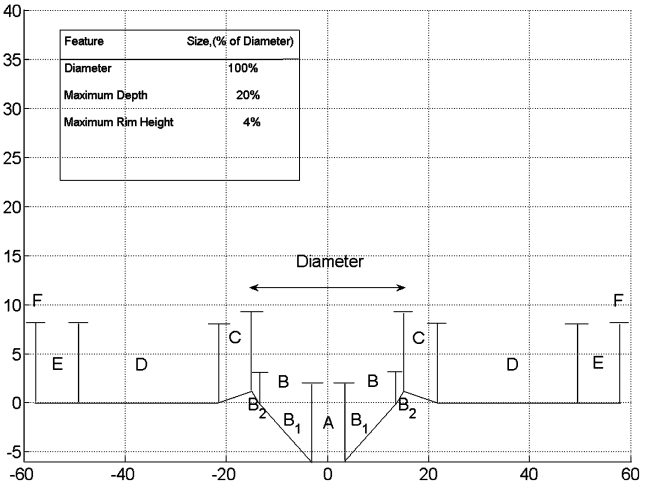

Fig. 19 Crater model cross section and crater scaling as determined by Bernard and Golombek [16].

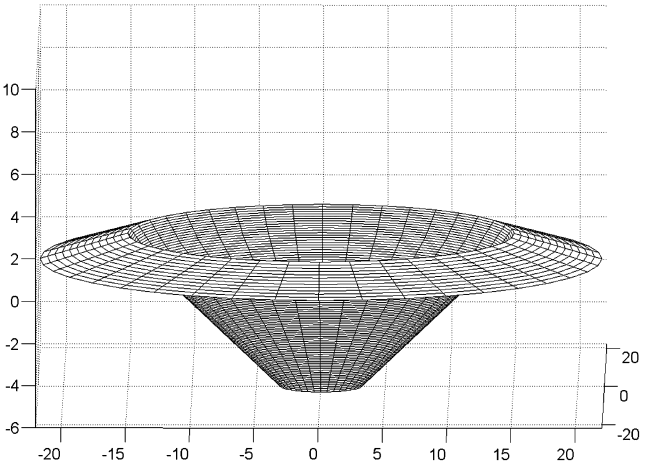

Fig. 20 Three-dimensional crater.

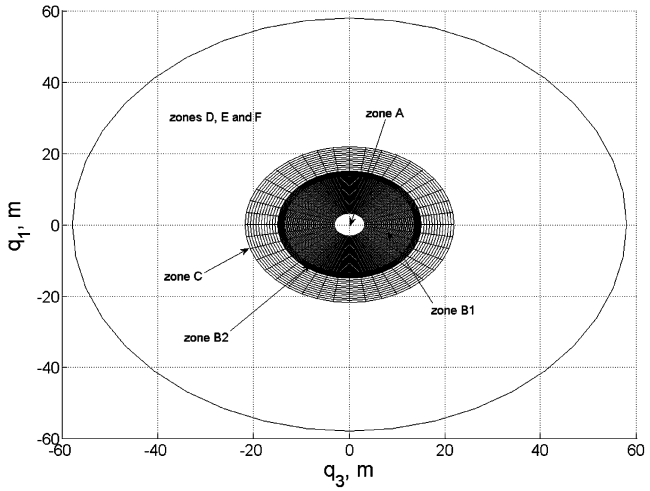

Fig. 21 Topographic view of a crater.

the result of the previous figure and also shows the rover rolling through the channel having an initial velocity magnitude equal in value to that in case I. Note that in both cases the initial translational and rotational kinetic energies are the same. The figure reveals that a rover colliding against a channel's wall may have the desired effect of propelling it further down a channel when compared to rolling alone. This result is attributed to the rover's energy loss during rolling, where the rolling resistance retards the rover's motion. Although the rover experiences friction during its contact phase of bouncing and rolling, the energy loss, when considering both modes of movement,

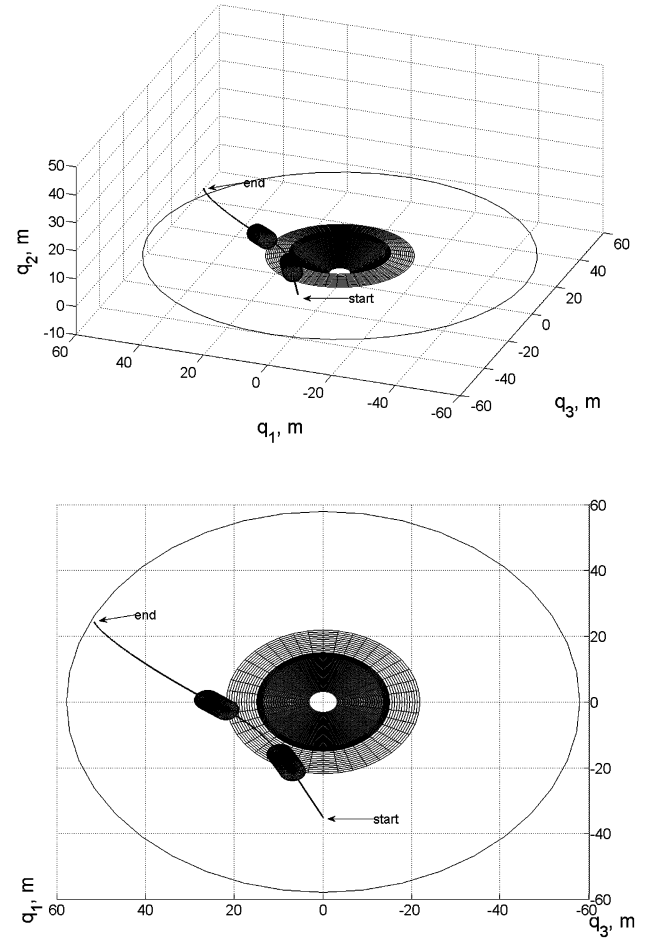

Fig. 22 Rover rolling off a crater's rim shown from two different viewpoints; circles denote bounce and the line denotes rolling/sliding.

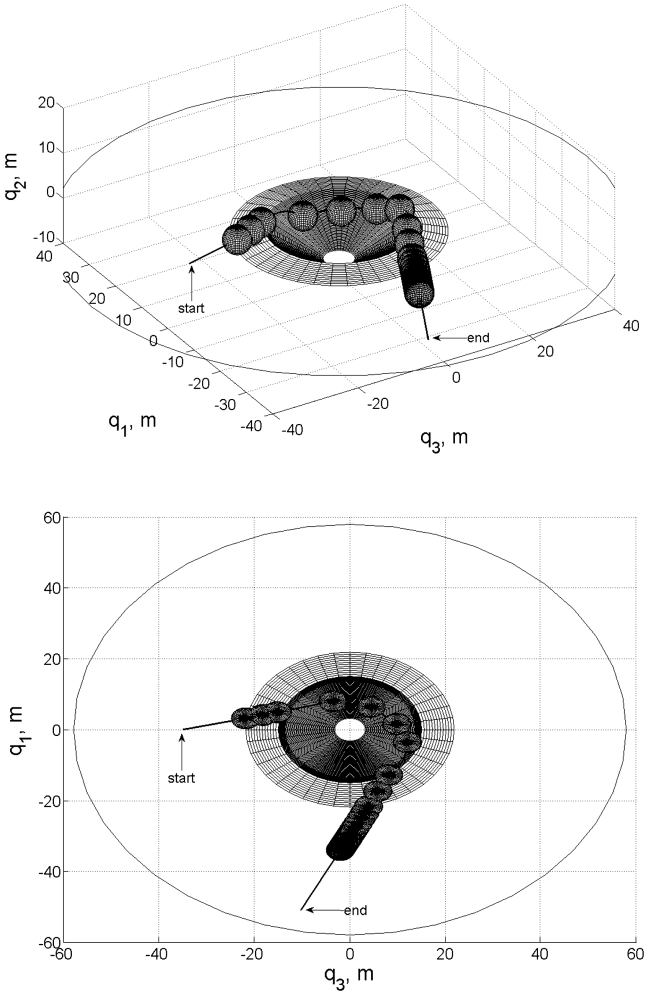

Fig. 23 Rover entering and exiting a crater shown from two different viewpoints; circles denote bounce and the line denotes rolling/sliding.

is mitigated by the rover being accelerated as it moves down the channel's side slope.

C. Example 3

The third example also concerns the behavior of a tumbleweed rover on Mars and seeks to accomplish two tasks. First, the general behavior of a rover as it encounters a crater is considered. Next, we examine the impact of aerodynamic effects on the capture of the rover by a crater.

A paper by Bernard and Golombek [16] showed that craters on Mars have a simple bowl shape with uplifted rims and dimensions that scale with crater diameter (see Fig. 19). The crater is divided into several zones: Zone A is the flat central region of the crater. Zone B is the crater's inner rim and is divided into two subregions, zone B1 and zone B2. Zone B1 has slopes of approximately 30°, and zone B2 has slopes greater than 30°. Zone C is the crater's outer rim having a slope of 10°. Zones D, E, and F are the areas external to the crater. Using the crater scaling laws described in [16], a three-dimensional crater is created. For a diameter of 30 m, Fig. 20 shows the crater's three-dimensional representation, and Fig. 21 presents a topographic view of the crater.

As a rover encounters a crater, it may behave in several different ways; these may be divided into three cases. Case 1 is when the rover fails to enter the crater, either bouncing or rolling off the crater's outer rim. Case 2 is when the rover enters and exits the crater through a series of bouncing and rolling combinations. Case 3 is when the rover is captured by the crater, i.e., where it settles out at the bottom of the crater. These cases are depicted in Figs. 22–24, respectively, for a crater having a diameter of 30 m. The atmospheric, gravitational, and rover properties for representative examples of each case along with

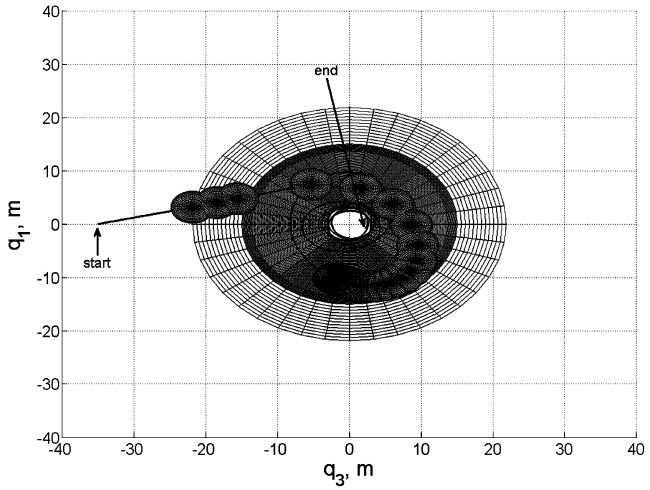

Fig. 24 Rover captured by a crater; circles denote bounce and the line denotes rolling/sliding.

other physical parameters and initial conditions are summarized in Table 3. For each case, the rover begins with a brief rolling phase before impacting the crater's outer rim. The rover is also given an initial velocity in both the q_1 and q_3 directions to ensure a three-dimensional interaction with the crater. For all cases the slope angles for zones B1 and B2 are 30 and 40°, respectively.

For case I, Fig. 22 shows the rover alternating between rolling and bouncing while moving on the crater's outer rim. Note that the rover's path deflection during its initial contact with the outer rim was large enough to prevent the rover's entry into the crater. Cases II and III show the rover entering the crater and illustrate the importance of including atmospheric effects in the simulation. Note that the exclusion of an atmosphere in the model allowed the rover to exit the crater (Fig. 23), whereas the inclusion of the drag and Magnus force resulted in the capture of the rover by the crater (Fig. 24), i.e., the aerodynamic effects prevented the rover from escaping the crater. In Fig. 24, we see that the rover failed to bounce out of the crater's inner rim (zone B2), and continued to bounce and roll before settling out at the crater's central region (zone A). Hence, this example demonstrates the importance of considering atmospheric effects when examining the possible capture of the rover by a crater.

IV. Conclusions

This paper formulates the equations governing the motion of a spherical rover and provides a numerical procedure for their implementation. Dynamic simulation models (considering both Earth and Mars atmospheres) for several terrain types and conditions are developed and illustrate how a rover may maneuver across flat terrain, a channel, or a crater. The results show that the wind force may both push and hinder the rover's motion while sliding, rolling, and bouncing. The rover will periodically transition between these modes of movement when the rover impacts sloped surfaces. Combinations of rolling and bouncing may be a more effective means of transport for a rover traveling through a channel when compared to rolling alone. The aerodynamic effects of drag and the Magnus force are contributing factors to the possible capture of the rover by a crater.

References

[1] Antol, J., Calhoun, P., Flick, J., Hajos, G., Kolancinski, R., Minton, D., Owens, R., and Parker, J., "Low Cost Mars Surface Exploration: The Mars Tumbleweed," NASA TM-2003-212411, Aug. 2003.

[2] Antol, J., Chattin, R. L., Copeland, B. M., and Krizan, S. A., "The NASA Langley Mars Tumbleweed Rover Prototype," 44th AIAA Aerospace Sciences Meeting, AIAA Paper 2006-0064, Reno, NV, Jan. 2005.

[3] Hajos, G., Jones, J., Behar A., and Dodd, M., "An Overview of Wind-Driven Rovers for Planetary Exploration," 43rd AIAA Aerospace Sciences Meeting and Exhibit, Reno, NV, AIAA Paper 2005-0245, Jan. 2005.

[4] Antol, J., Calhoun, P., Flick, J., Hajos, G., Keyes, J., Stillwagen, F., Krizan, S., Strickland, C., Owens, R., and Wisniewski, M., "Mars Tumbleweed: FY2003 Conceptual Design Assessment," NASA TM-2005-213527, Aug. 2005.

[5] Antol, J., "A New Vehicle for Planetary Surface Exploration: The Mars Tumbleweed," 1st Space Exploration Conference: Continuing the Voyage of Discovery, AIAA Paper 2005-2520, Orlando, FL, 2005.

[6] Flick, J. and Toniolo, M., "Preliminary Dynamic Feasibility and Analysis of a Spherical, Wind Driven (Tumbleweed) Martian Rover," 43rd AIAA Aerospace Sciences Meeting and Exhibit, AIAA Paper 2005-0250, Reno, NV, Jan. 2005.

[7] Lorenz, R., Behar, A., Nicaise, F., Jonsson, J., and Myers, M., "Field Testing and Dynamic Model Development for a Mars Tumbleweed Rover," *Proceedings of the 4th International Planetary Probe Workshop*, Pasadena, CA, June 2006, http://ippw.jpl.nasa.gov/20070607_doc/8_9LOREN.pdf [retrieved 8 January 2009].

[8] Wilson, J. L., Mazzoleni, A. P., DeJarnette, F. R., Antol, J., Hajos, G. A., and Strickland, C. V., "Design, Analysis, and Testing of Mars Tumbleweed Rover Concepts," *Journal of Spacecraft and Rockets*, Vol. 45, No. 2, March–April 2008, pp. 370–382. doi:10.2514/1.31288

[9] Hartl, A. E. and Mazzoleni, A. P., "Parametric Study of Spherical Rovers Crossing a Valley," *Journal of Guidance, Control, and Dynamics*, Vol. 31, No. 3, May–June 2008, pp. 775–779. doi:10.2514/1.33932

[10] Kane, T. R. and Levinson, D. A., "Extraction of Information from Equations of Motion," *Dynamics: Theory and Applications*, McGraw–Hill, New York, 1985, pp. 233–239.

[11] Fowles, G. R. and Cassiday, G. L., "General Motion of a Particle in Three Dimensions," *Analytical Mechanics*, Saunders College Publishing, Fort Worth, TX, 1999, pp. 145–153.

[12] Fox, R. W., McDonald, A. T., and Pritchard, P. J., "External Incompressible Viscous Flow," *Introduction to Fluid Mechanics*, Wiley, New York, 2003, pp. 461–465.

[13] Bacon, M. E., "How Balls Roll Off Tables," *American Journal of Physics*, Vol. 73, No. 8, Aug. 2005, pp. 722–724. doi:10.1119/1.1947198

[14] Rose, S., Moody, C., James, D. L., and Barhorst, A. A., "Drag Measurement and Dynamic Simulation of Martian Wind Driven Sensor Platform Concepts," *Journal of Fluids and Structures*, Vol. 22, No. 1, Jan.. 2006, pp.21–43. doi:10.1016/j.jfluidstructs.2005.09.008

[15] White, F. M, "Efficient Uniform-Flow Channels," *Fluid Mechanics*, McGraw–Hill, New York, 2003, pp. 702–704.

[16] Bernard, D. E. and Golombek, M. P., "Crater and Rock Hazard Modeling For Mars Landing," *AIAA Space 2001 Conference and Exposition*, AIAA Paper 2001-4697, Albuquerque, NM, Aug. 2001.

D. Spencer
Associate Editor